PCCP

Accepted Manuscript

PCCP

ARTICLE

Supercapacitive Behavior Depending on Mesopore Size of Three-Dimensional Micro-, Meso- and Macroporous Silicon Carbide for Supercapacitors

Myeongjin Kim, Ilgeun Oh and Jooheon Kim*

Three-dimensional silicon carbide-based frameworks with hierarchical micro-, meso-, and macroporous structures (3MPSiC) were prepared by a template method with subsequent carbonization via an aerosol spray drying method. The micropores were derived from partial vaporization of Si atoms during the carbonization process, whereas the meso- and macropores were generated by self-assembly of the structure directing agent and polystyrene latex spheres, respectively. The effect of the mesopore size on the electrochemical performance of 3MPSiC electrodes was evaluated by fabricating three types of 3MPSiC samples with different mesopore size by using three different structure directing agents (cetyltriethylammonium bromide (CTAB), Polyethylene glycol hexadecyl ether (Brij56), and Poly(ethylene glycol)-*block*-poly(propylene glycol)-*block*-poly(ethylene glycol) (P123)). The 3MPSiC electrode prepared with Brij56 exhibited outstanding electrochemical performance with a specific capacitance of 336.5 F g^{-1} at a scan rate of 5 mV s^{-1} with 90.3 % rate performance from 5 to 500 mV s^{-1} in 1 M Na_2SO_4 aqueous electrolyte. The outstanding electrochemical performance is attributed to the ideal mesopore size that can effectively reduce resistant pathways for ion diffusion in the pores as well as provide a large accessible surface area for ion transport/charge storage. These encouraging results demonstrate the high potential of 3MPSiC prepared with Brij56 for application as a high-performance electrode material for supercapacitors.

1. Introduction

The rapid development of renewable energy sources, including solar and wind power harvesting devices, has increased the need for sustainable energy storage technologies in order to address the challenges of increasing energy demand and the cyclic nature of renewable energy sources.[1-3] Because of their high power density, moderate energy density, good operational safety, and long cycling life, electrochemical double-layer capacitors or supercapacitors have been extensively explored and have gained recognition as promising devices for various emerging energy applications in high-power electronics, electric vehicles, and hybrid electric vehicles.[4-7]

Generally, supercapacitors are classified into one of two categories based on their energy-storage mechanism, i.e., electric double-layer capacitors (EDLCs) and pseudocapacitors.[8] Pseudocapacitors store electrical energy faradaically by electrosorption, reduction-oxidation reactions, and intercalation processes. However, practical application of pseudocapacitors is limited due to the inherent low electrical conductivity and poor cycle stability.[9] Energy storage by EDLCs is generally based on the adsorption of electrolyte ions on large specific surface area conductive electrodes, where the surface charge is separated at electrode/electrolyte interfaces.[10,11] Therefore, high surface areas and

pores that are adapted to the size of the electrolyte ions are required for EDLCs. In this regard, various types of porous carbon-based materials, such as activated carbon, carbide-derived carbons, ordered mesoporous carbons, and carbon aerogels, have been studied as high surface area electrodes.[12-17] However, the low electrical conductivity of these materials is not favorable for construction of the conductive network; the low electrochemical resistance may decrease the internal resistance of the electrode and generate electrostatic charges on the surface of the electrode, thereby forming the electric double layer.[18]

Because of the large theoretical surface area (~2630 m^2 g^{-1}), excellent electronic conductivity, outstanding chemical stability, and good physical properties of graphene, many studies have investigated the use of graphene as an EDLC material.[19-22] However, in practice, the surface area of chemically obtained graphene is much lower than the theoretical surface area due to incomplete exfoliation of graphene oxide and coalescence during the reduction process.[23] Thus, the development of new candidate electrode materials with high surface area and electrical conductivity is essential. A number of approaches have been proposed for the application of semiconductors or cermet nanowires as EDLC electrode materials instead of traditional carbon-based materials. Various types of EDLC materials, such as silicon nanowires, silicon carbide

nanowires, titanium nitride nanowires, and titanium dioxide nanotubes and nanowires, have attracted considerable interest because of their high surface area and excellent electrical conductivity.[24-29] Silicon carbide, and nanowire type silicon carbide in particular, have distinguishing potential as EDLC materials due to their high electron mobility and low band gap combined with high surface area. However, these nanowire structures are desirable not only for fabrication of hybrid composites combined with metal oxide or conductive polymers but also for application as macroscale supercapacitor electrodes given that the working materials are grown directly on the current collector.

Recently, the use of silicon carbide microsphere particles as EDLC materials has been reported, and their potential as candidate EDLC materials has been demonstrated. However, the porous properties, such as the surface area and pore volume, of these silicon carbide microsphere particles is not impressive due to the non-porous structure, resulting in low capacitive performance (72.4 F g^{-1} at a scan rate of 10 mV s^{-1} in Na_2SO_4 aqueous electrolyte).[30-32] Consequently, in order to obtain high surface area, it is crucial to develop silicon carbide particles with porous structures that can provide efficient ion-accessible surface area for charge storage. To achieve this, the relationship between the pore structure of EDLC materials and the electrochemical capacitive behavior must be considered. The pores can be classified into three categories depending on their size, and each pore type plays a unique role in the charge/discharge process. Macropores serve as ion-buffering reservoirs, giving rise to a decreased diffusion distance; mesopores provide ion-transport pathways with minimized resistance, and micropores enhance the electrical double layer.[33-36] Therefore, the combination of these three kinds of pores in EDLC materials is expected to provide a harmonious electrochemical environment for the full realization of fast ion transport and high charge storage capability.[33]

In this study, a novel hierarchical micro-, meso-, and macroporous silicon carbide (3MPSiC) sphere is developed using a template method followed by carbonization via an aerosol spray drying method. The mesopores play an important role in this ternary pore system, providing low-resistance pathways for ion diffusion in the pores as well as a large accessible surface area for ion transport/charge storage. To achieve fundamental insight into the electrode kinetic mechanisms and the correlation between the porous structure and electrolyte ions, it is important to investigate the relationship between the mesopore size and electrochemical performance. Therefore, three kinds of 3MPSiC with different mesopore sizes are fabricated herein by using three different structure directing agents (cetyltriethylammonium bromide (CTAB), Polyethylene glycol hexadecyl ether (Brij56), and Poly(ethylene glycol)-*block*-poly(propylene glycol)-*block*-poly(ethylene glycol) (P123)). The 3MPSiC electrode prepared with Brij56 is demonstrated to exhibit high charge storage capacity with a specific capacitance of 336.5 F g^{-1} at a scan rate of 5 mV s^{-1} with 90.3 % rate performance from 5 to 500 mV s^{-1} in 1 M Na_2SO_4 aqueous electrolyte. These encouraging results indicate that the micro-, meso-, and macroporous silicon carbide prepared using Brij56 as a mesopore template possess potential advantages for application as supercapacitor electrodes with high energy and power density.

2. Experimental

2.1 Preparatoin of Polystyrene Latex (PSL) Spheres

A batch reactor with reflux was used to prepare monodisperse polystyrene spheres. In the reactor, 0.0975 g of sodium salt of dodecyl sulfate (SDB-Na), 0.325 g of potassium peroxodisulfate ($K_2S_2O_8$), and 32.5 mL of styrene monomer were dissolved in 186.5 mL D.I. water. Polymerization was carried out with magnetic stirring at 80° C for 18 hours. Monodisperse PSL spheres 80 nm in diameter were prepared in suspension. Sols with various concentrations of PSL were formed by diluting the as-prepared suspension (14.8 wt% PS) with D.I. water.

2.2 Synthesis of Micro-, Meso- & Macroporous Silicon Carbide (3MPSiC)

In a typical synthesis, 0.917 g of silicon nanoparticles (about 5 nm) was dispersed in 33 mL of D.I. water. Subsequently, 0.014 mL of hydrogen chloride (HCl), 43.3 mL of ethanol (C_2H_5OH), and x g of structure directing agent (value of x is indicated in brackets in the following sentence) were added, followed by stirring for 1 h. $C_{16}H_{33}N(CH_3)_3Br$, CTAB (x = 1.8223 g); $C_{16}H_{33}(EO)_{10}$, Brij56 (x = 1.9742 g), and $(EO)_{20}(PO)_{70}(EO)_{20}$, P123 ($x$ = 2.2467 g) were respectively used as structure directing agents. Finally, the 14.8 wt% PSL suspension was added in a volume ratio of 1:1 and stirred for 2 h. The samples were denoted as 3MPSiC-C, 3MPSiC-B, and 3MPSiC-P based on the type of structure directing agent employed, corresponding to CTAB, Brij56, and P123, respectively. The resulting solution mixtures were ultrasonically sprayed using a home humidifier (60 MHz and 35 W). The droplets were carried by argon (Ar) gas (purity: 99.999%) at a flow rate of 100 sccm (standard cubic centimeter per minute) into a tubular reactor. The tubular reactor is separated into two segments, the drying and heating zones. The drying zone of the tubular reactor (30 mm in diameter and 700 mm in length) was heated to 150°C, and the heating zone of the tubular reactor (30 mm in diameter and 1000 mm in length) was heated to 1250°C. At the entrance of the heating zone, C_2H_5OH was ultrasonically carried by Ar gas at a flow rate of 60 sccm. The particles were recovered via filtration at the outlet of the heating zone tubular reactor. After the reaction was terminated and the reactor was cooled to room temperature, the resulting products were exposed to air and heated at 600°C for 4 h to remove the excess carbon. Finally, the adsorbed SiO_2 layer on the surface of the 3MPSiC particles was removed via treatment with hydrofluoric acid (HF). 10 g of 3MPSiC powder was placed in 300 mL of 10% HF solution and stirred for 24 h. Subsequently, the sample was leached with distilled water until the pH of the leaching water reached 7–8.

2.3 Characterization Methods

X-ray diffraction (XRD) patterns were collected (New D8-Advance/Bruker-AXS) at a scan rate of 1° s^{-1} within the 2θ range 10°–80° using $CuK_{\alpha1}$ radiation (0.154056 nm). The morphologies of the samples were observed using high-resolution transmission electron microscopy (HR-TEM, JEM-3010). X-ray photoelectron

spectroscopy (XPS) analysis was performed on a VGMicrotech ESCA2000 system using a spectrometer with a Mg Kα X-ray source (1253.6 eV) and a hemispherical analyzer. During the curve fitting, the Gaussian peak widths were constant in each spectrum. Nitrogen sorption analysis was carried out using an ASAP 2020 accelerated surface area and porosimetry instrument (Micromeritics), equipped with an automated surface area at 77 K, using Brunauer–Emmett–Teller (BET) calculations for the surface area. The pore-size distribution plots were recorded from the desorption branch of the isotherms based on the nonlocal density functional theory (DFT).

2.4 Preparation and Characterization of Supercapacitors

Working electrodes were fabricated as follows: first, the as-prepared materials, carbon black and poly(vinylidenefluoride) (PVDF) were mixed in a mass ratio of 85:10:5 and dispersed in *N*-methylpyrrolidone (NMP). The resulting mixture was then coated onto an aluminum foil substrate (1 cm × 1 cm) and dried in a vacuum oven at 60°C for 6 h. The loading mass of each electrode was approximately 2.7–3.2 mg. In a three-electrode cell, the above-loaded aluminum foil substrate, a platinum foil, and a Ag/AgCl (KCl-saturated) electrode were used as the working, counter, and reference electrodes, respectively. All measurements, including cyclic voltammetry (CV), galvanostatic charge/discharge characteristics, and Electrochemical impedance spectroscopy (EIS) measurements, were performed using a CHI 660C electrochemical workstation, in 1 M Na_2SO_4 aqueous solution, at room temperature. EIS measurements were carried out by applying an AC voltage with 5 mV amplitude in the frequency range of 0.01 to 10^5 Hz at open-circuit potential.

3. Results and Discussion

The procedure for synthesis of the micro-, meso-, and macroporous silicon carbide (3MPSiC) sphere is illustrated in Scheme 1. A mixture of the respective structure directing agents (CTAB, Brij58, or P123), polystyrene latex (PSL) spheres, and an aqueous suspension of small silicon particles (about 5 nm) was ultrasonically sprayed into the tubular reactor with two different reactor temperature segments (drying zone (150 °C) and heating zone (1250 °C)). Ethanol, which was used as a carbon source, was sprayed at the entrance of the heating zone and carried by argon gas. In the drying zone, when the solvent evaporates from the solution
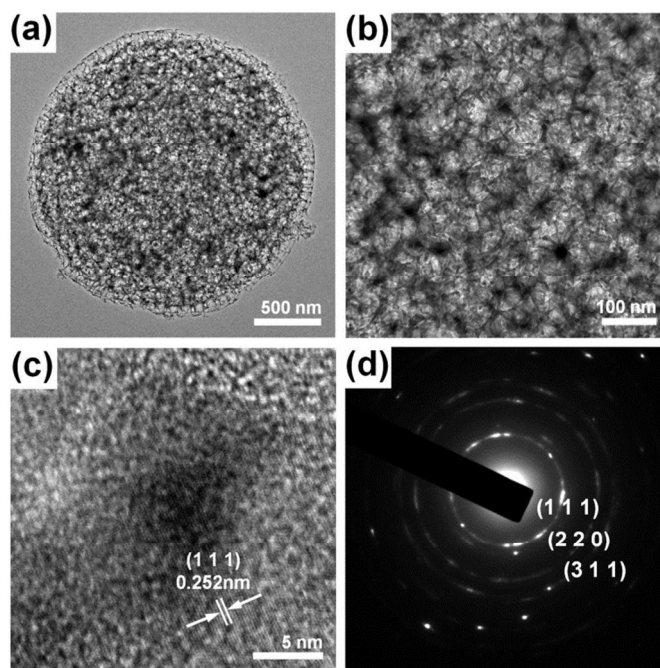
Figure 1. (a) Low-magnification FE-TEM image of 3MPSiC-B. (b,c) High-magnification FE-TEM image of 3MPSiC-B. (d) SAED pattern of 3MPSiC-B.

mixtures, the PSL spheres self-assemble into a face-centered cubic (FCC) colloidal crystal, then the hexagonal aligned Brij56 micellar rod is allowed to infiltrate the spaces between the PSL spheres. In the meantime, the silicon particles are trapped in the voids of the agglomerated PSL particles and Brij56 micellar rod, leading to formation of silicon walls.[37-39] In the heating zone, both the Brij56 micellar rod and PSL are removed, resulting in the formation of ordered hexagonal arrangement of mesopores with FCC arrangement of macropores, and then the resulting meso- and macroporous Si sphere frames are converted to micro-, meso- and macroporous SiC spheres via carbonization, using ethanol as the carbon source.[40]

The microstructural images of 3MPSiC are shown in Figure 1. The High resolution transmission electron microscopy (HR-TEM) (Figure 1(a) and (b), S1(a) and (b), S2(a) and (b)) showed that the 3MPSiC possesses a highly porous structure with a large fraction of open, interconnected, macropores in a three-dimensional framework, and the macroporous walls are composed of disordered mesopores. The hexagonal, aligned mesopores in the Si sphere frames collapse and become integrated with neighboring mesopores during the
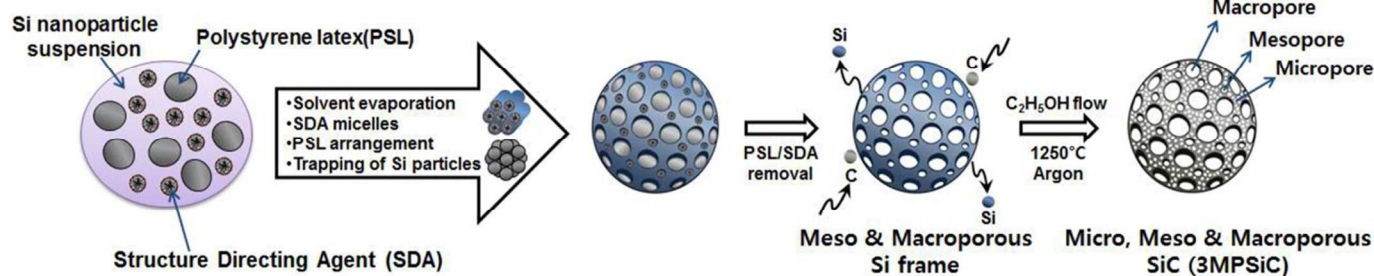
Scheme 1. Chemical route for the synthesis of 3MPSiC.

carbonization process due to partial vaporization of the Si atoms in the walls of the ordered mesopores. Furthermore, as shown in Figure 1(c), S1(c) and S2(c), 3MPSiC possesses a large fraction of micropores with random orientation. The formation of the micropores on meso- and macroporous SiC can be attributed to partial vaporization of Si atoms from the meso- and macroporous Si sphere frames and carbonization of the remaining micro-, meso-, and macroporous Si sphere frames at high temperature. At the heating temperature of 1250 °C, some of the Si atoms are released from the meso- and macroporous Si sphere frames with consequent formation of micropores, leading to formation of micro-, meso-, and macroporous Si sphere frames. The remaining micro-, meso-, and macroporous Si sphere frames react with active carbon species decomposed from C_2H_5OH to form micro-, meso-, and macroporous SiC spheres. After carbonization, the mother meso- and macroporous Si spheres were completely converted into micro-, meso-, and macroporous SiC spheres.[40] The overall structure consists of micro- and mesopores within an interconnected macroporous network, which is expected to provide high permeability towards electrolyte ions.[11] In order to confirm the successful conversion of silicon carbide, the crystalline structure of 3MPSiC was evaluated. The lattice fringes (Figure 1(c), S1(c) and S2(c)) with interplanar distances of approximately 0.252 ± 0.01 nm correspond to the (1 1 1) plane of the β-SiC structure.[41] In addition, Figure 1(d), S1(d) and S2(d) is the selected area electron diffraction (SAED) pattern of shells with three clear diffraction rings corresponding to the (1 1 1), (2 2 0), and (3 1 1) diffraction planes of β-SiC, providing further evidence that the converted 3MPSiC is composed of well-crystallized β-SiC nanocrystals.[42]
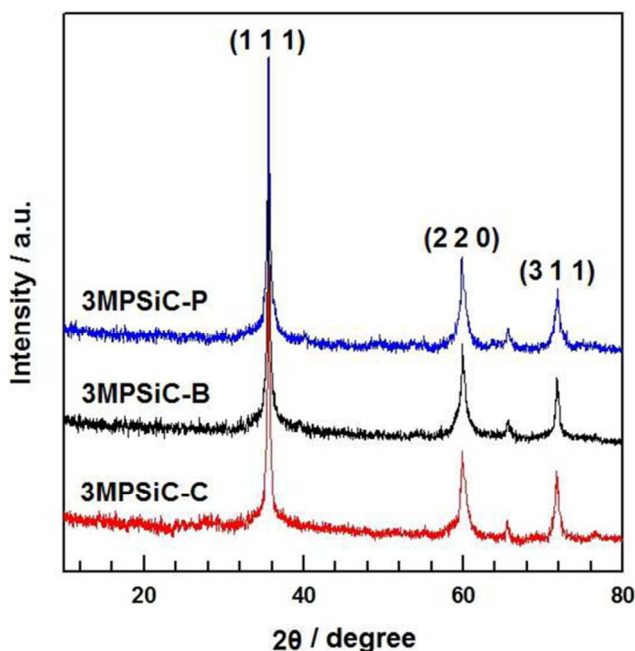
Figure 2. XRD patterns of 3MPSiC-C, 3MPSiC-B and 3MPSiC-P.

Figure 2 shows the X-ray diffraction (XRD) patterns of 3MPSiC-C, 3MPSiC-B, and 3MPSiC-P. The XRD patterns of 3MPSiC-C, 3MPSiC-B, and 3MPSiC-P show three β-SiC peaks at 2θ = 35.6°, 60°, and 71.7°, which were assigned to the (1 1 1), (2 2 0), and (3 1

1) reflections, respectively. These were correlated to the face-centered cubic (fcc) β-SiC structure in accordance with the reference data (JCPDS 29-1129, a = 4.3589 Å), which is consistent with SAED results.[41,42] In addition, the d-spacing of the (1 1 1) plane is calculated to be 0.252 nm, which is in good agreement with the lattice interlayer distance observed by TEM analysis. The electrical conductivity of 3MPSiC-C, 3MPSiC-B, and 3MPSiC-P that was determined for pressed pellets using the four-probe method was quantified as 112.4, 117.2, and 120.3 S cm^{-1}, respectively; these values are much higher than that of commercialized activated carbon (0.1 ~ 1 S cm^{-1}), activated carbon fibers (5 ~ 10 S cm^{-1}) and carbon aerogels (1 ~ 10 S cm^{-1}).[18] The excellent electrical conductivity of 3MPSiC is attributed to the β-polytype crystalline structure of as-synthesized 3MPSiC. It is well known that the β-polytype of SiC exhibits the highest electronic conductivity among the SiC polytypes because β-SiC possesses the smallest bandgap (~2.4 eV) and one of the highest electron mobilities (~800 cm^2 V^{-1} s^{-1} in low-doped material).[43]

Detailed surface analysis of 3MPSiC-C, 3MPSiC-B, and 3MPSiC-P was performed using X-ray photoelectron spectroscopy (XPS), as shown in Figure 3. The XPS survey spectrum of 3MPSiC-C, 3MPSiC-B, and 3MPSiC-P (Figure 3(a)) consisted of only three elements, namely C, Si, and O. To obtain the detailed surface information, the Si 2p, C 1s, and O 1s core-level spectra of each sample were deconvoluted; the results are shown in Figure 3(b)–(d) and S3, S4 and summarized in Table S1 and S2. Moreover, the relative atomic percentage was obtained by taking the ratio of each of the peak areas in the Si 2p, C 1s, and O 1s core-level spectra. The Si 2p region of the spectrum acquired from the surface of 3MPSiC (Figures 3(b), S3(a), and S4(a)) showed that in addition to the strong Si–C peak at the binding energy of 99.5 eV, some intermediate oxidation products of SiC were also present on the surface. These were interpreted as $SiOC_3$ at 100.4 eV, SiO_2C_2 at 101.3 eV and SiO_3C at 102.1 eV.[44] The C 1s core level (Figures 3(c), S3(b), and S4(b)) showed strong binding energy peaks of Si–C bonds at 282.8 eV and C–C bonds at 284.6 eV, with several binding energy peaks of SiO_xC_y at 283.7 ~ 283.8 eV. In the O 1s spectra (Figures 3(d), S3(c), and S4(c)), a SiO_xC_y peak was present at the binding energy of 532.2 eV.[45]

The hierarchical micro-, meso-, and macroporous features of 3MPSiC were further confirmed by nitrogen adsorption-desorption measurements. Brunauer-Emmett-Teller (BET) and density functional theory (DFT) analyses were employed to investigate the surface area and pore structure of 3MPSiC; the results are presented in Figure 4 and the porous properties of the resultant 3MPSiC are summarized in Table 1. The porosity of the resultant 3MPSiC was significantly influenced by the structure directing agents. It can be clearly seen that all of the 3MPSiC samples exhibited similar trends in the adsorption and desorption isotherms (Figure 4(a)). The adsorption amount increased very sharply at low relative pressure (P/P_o), demonstrating the existence of micropores; a hysteresis loop is observed after P/P_o = 0.4, but no adsorption plateau is apparent near P/P_o = 1.0, indicating the presence of meso- and macropores.[33,35] The total specific surface areas of 3MPSiC-C, 3MPSiC-B, and 3MPSiC-P were calculated to be above 2544, 2302,
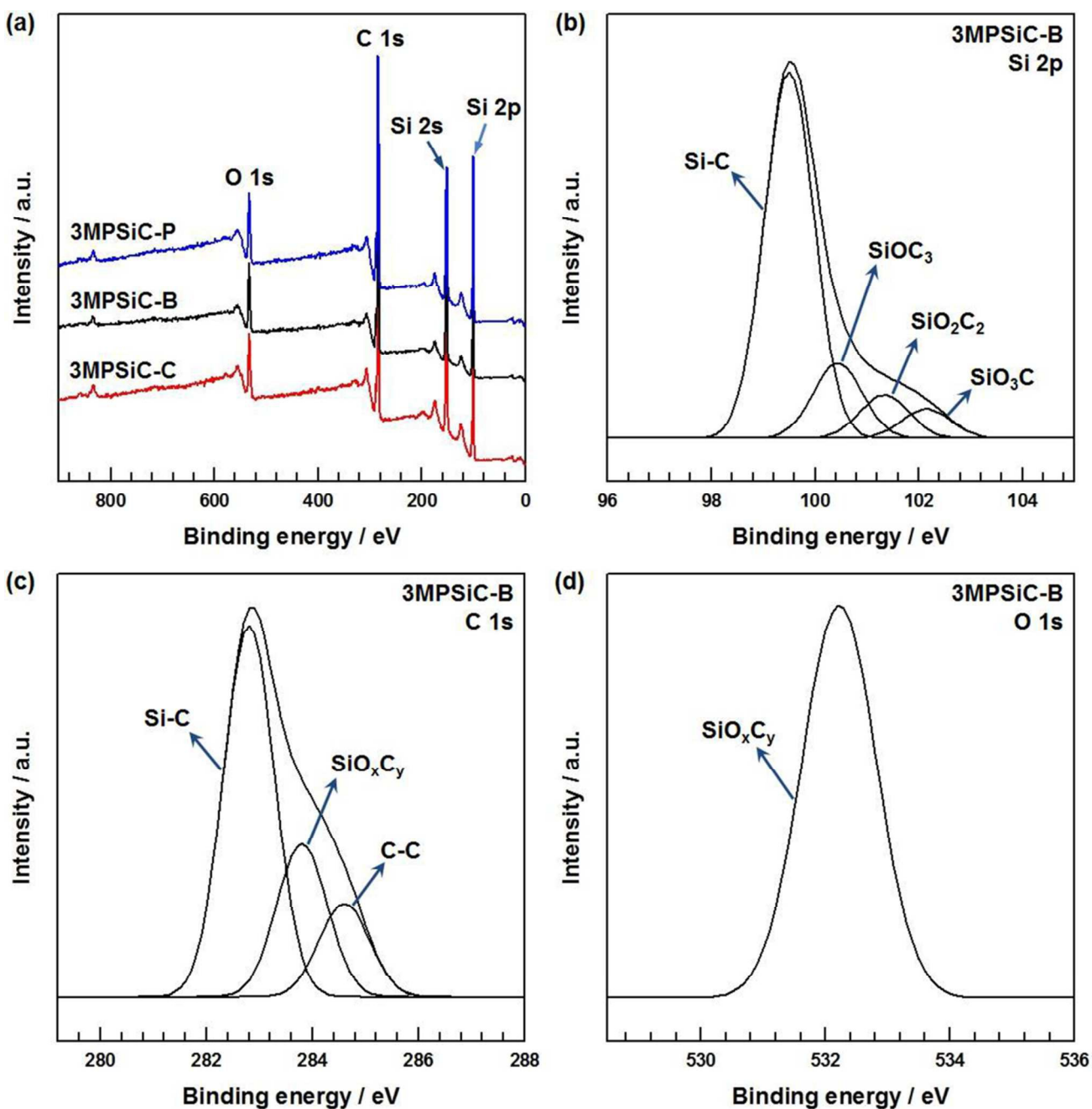
Figure 3. (a) XPS wide scan survey spectra of 3MPSiC-C, 3MPSiC-B and 3MPSiC-P. (b) Deconvoluted Si 2p spectra of 3MPSiC-B. (c) Deconvoluted C 1s spectra of 3MPSiC-B. (d) Deconvoluted O 1s spectra of 3MPSiC-B.

and 2076 m^2 g^{-1}, respectively. The differences in the specific surface areas of the 3MPSiC samples are attributed to the dependence of the mesopore surface area on the structure directing agents. To evaluate the effects of the structure directing agents, the pore size distributions of 3MPSiC-C, 3MPSiC-B, and 3MPSiC-P were analyzed as shown in Figure 4(b). It reveals that the nanopores of all of the 3MPSiC can be divided into three major regions, namely micropores (pore diameter < 2 nm), mesopores (2 nm < pore diameter < 50 nm) and macropores (pore diameter > 50 nm). In the

micropore and macropore regions, all of the 3MPSiC exhibits similar distribution with similar pore volume because of the same carbonization environments and same PSL sphere size and contents. However, in the mesopore region, the order of the mesopore size ranks as: 3MPSiC-P > 3MPSiC-B > 3MPSiC-C, which is in accordance with increasing volume/molecular mass of the structure directing agent (P123 > Brij-56 > CTAB).[38] Therefore, the mesopore surface area follows the order: 3MPSiC-C (681 m^2 g^{-1}) > 3MPSiC-B (429 m^2 g^{-1}) > 3MPSiC-P (203 m^2 g^{-1}) given that a smaller pore size leads to higher surface area. In this regard, it can be expected that the

difference in the mesopore surface area and pore volume properties of the 3MPSiC samples can lead to differences in the ion transport behavior, giving rise to different electrochemical performance.
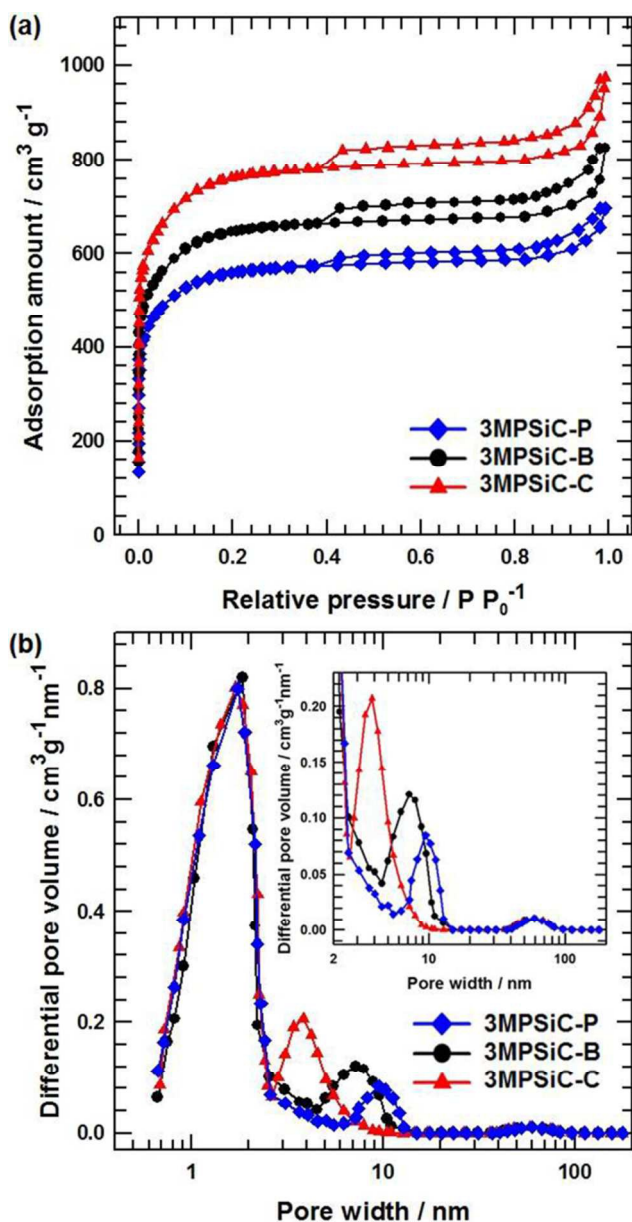
Figure 4. (a) Nitrogen adsorption-desorption isotherm of 3MPSiC-C, 3MPSiC-B and 3MPSiC-P. (b) Pore-size distribution of 3MPSiC-C, 3MPSiC-B and 3MPSiC-P. (the inset illustrates meso- and macropore region)

To explore the potential applicability in supercapacitors, the samples were fabricated into supercapacitor electrodes and were characterized via cyclic voltammetry (CV), galvanostatic charge/discharge, and electrochemical impedance spectroscopy. Figure 5(a) shows the CV curves of the 3MPSiC-C, 3MPSiC-B, and 3MPSiC-P electrodes, acquired with potential windows ranging from –0.1 to 0.9 V (vs. Ag/AgCl), at a scan rate of 5 mV s^{-1}, in 1 M Na$_2$SO$_4$ aqueous solution. Generally, for an ideal porous EDLC
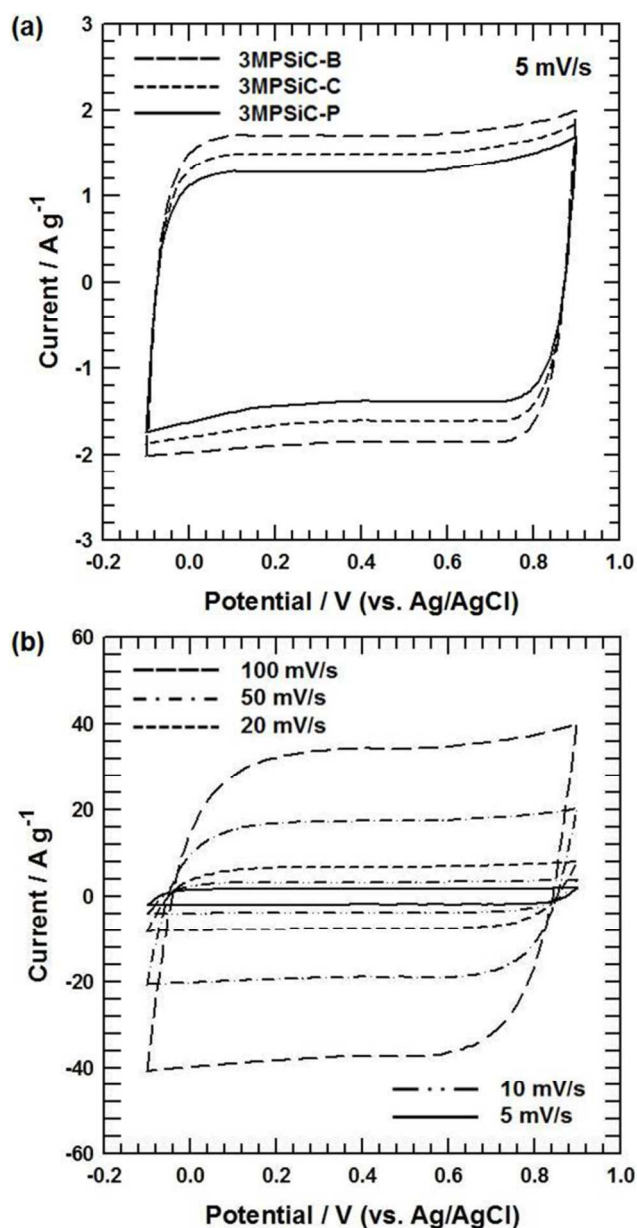
Figure 5. (a) CV curves for 3MPSiC-C, 3MPSiC-B and 3MPSiC-P electrodes at a scan rate of 5 mV s^{-1}. (b) CV curves of 3MPSiC-B electrode at different scan rates.

electrode, the nanopore structure will have a short ion diffusion distance and provide fast ion transport pathways. In this case, the electrical double layer can be reorganized rapidly at the switching potentials, and then the response current reaches a steady state, resulting in rectangular-shaped CV curves. Therefore, the rectangular shape can be used to estimate the ion transfer/diffusion rate within the porous structure, where the more rectangular the curve, the faster the ion transport.[33] The CV profiles for all 3MPSiC electrodes have an almost rectangular shape, suggesting that all of the evaluated 3MPSiC electrodes have satisfactory ion transfer/diffusion response.[46] The excellent electrochemical properties of the 3MPSiC electrodes are attributed to the following: (i) the interconnected macropores within the frameworks are

Table 1. Pore characteristics of 3MPSiC-C, 3MPSiC-B and 3MPSiC-P.

	S_{BET} [m^2 g^{-1}]	S_{micro} [m^2 g^{-1}]	S_{meso} [m^2 g^{-1}]	S_{macro} [m^2 g^{-1}]	V_{tot} [cm^3 g^{-1}]	V_{micro} [cm^3 g^{-1}]	V_{meso} [cm^3 g^{-1}]	V_{macro} [cm^3 g^{-1}]
3MPSiC-C	2544	1844	681	19	1.816	0.825	0.652	0.339
3MPSiC-B	2302	1852	429	21	1.945	0.838	0.771	0.336
3MPSiC-P	2076	1850	203	23	1.642	0.832	0.482	0.328

favorable for the formation of an ion buffering reservoir to minimize the diffusion distances from the external electrolyte to the interior surfaces; (ii) the mesopores of 3MPSiC provide low-resistance pathways for ion diffusion in the pores, which leads to improved capacitive activity; (iii) the abundant micropores play an essential role for optimizing the electrical double-layer surfaces and thus enhance the capacitance; (iv) the high surface area and pore volume of 3MPSiC derived from the mixed pore system (micro/meso/macroporous) is favorable for furnishing electrochemically available surface area for charge accumulation, resulting in high specific capacitance; (v) the excellent electrical conductivity of 3MPSiC can significantly decrease the internal resistance of the electrode via construction of a conductive network and facilitate application of electrostatic charges that are favorable for accumulating the electric double layers.[33-36] Although the specific surface area of 3MPSiC-B is smaller than that of 3MPSiC-C, a much larger integrated area was obtained in the CV curve of the 3MPSiC-B electrode, indicating that the 3MPSiC-B electrode exhibits much higher specific capacitance than the 3MPSiC-C electrode. This is attributed to the fact that the mesopore size of 3MPSiC-B is larger than that of 3MPSiC-C, which is highly beneficial for electrolyte access into the pores and for ion transport.[36] Comparison of the 3MPSiC-C and 3MPSiC-P electrodes shows a much larger integrated area in the CV curve of the former due to the much higher mesopore surface area and volume. The high surface area and pore volume are favorable properties for furnishing electrochemically available surface area for charge accumulation for generating a larger number of double layers, resulting in high capacitive performance.[47] The capacitive performance was further assessed by subjecting the 3MPSiC-B electrode to detailed measurements. Figure 5(b) shows the CV curves of the 3MPSiC-B electrode acquired at scan rates of 5, 10, 20, 50, and 100 mV s^{-1} in 1 M Na$_2$SO$_4$ aqueous solution. The CV profiles retain a largely rectangular shape with high symmetry and do not show any signs of obvious distortion with increasing potential scan rate, indicating that the 3MPSiC-B electrode has ideal capacitive properties and excellent reversibility.[48]

Galvanostatic charge/discharge measurements of the 3MPSiC-C, 3MPSiC-B, and 3MPSiC-P electrodes were carried out in 1 M Na$_2$SO$_4$ solution, in the range of -0.1 to 0.9 V, at a current density of 1 A g^{-1}. As shown in Figure 6(a), the charge curves of all the 3MPSiC electrodes during the charging and discharging steps are almost symmetric to their corresponding discharge counterparts, indicating the electric double-layer contribution due to the connective porous structure.[49] Moreover, comparison of the discharge curves shows that the discharge time is longest for the
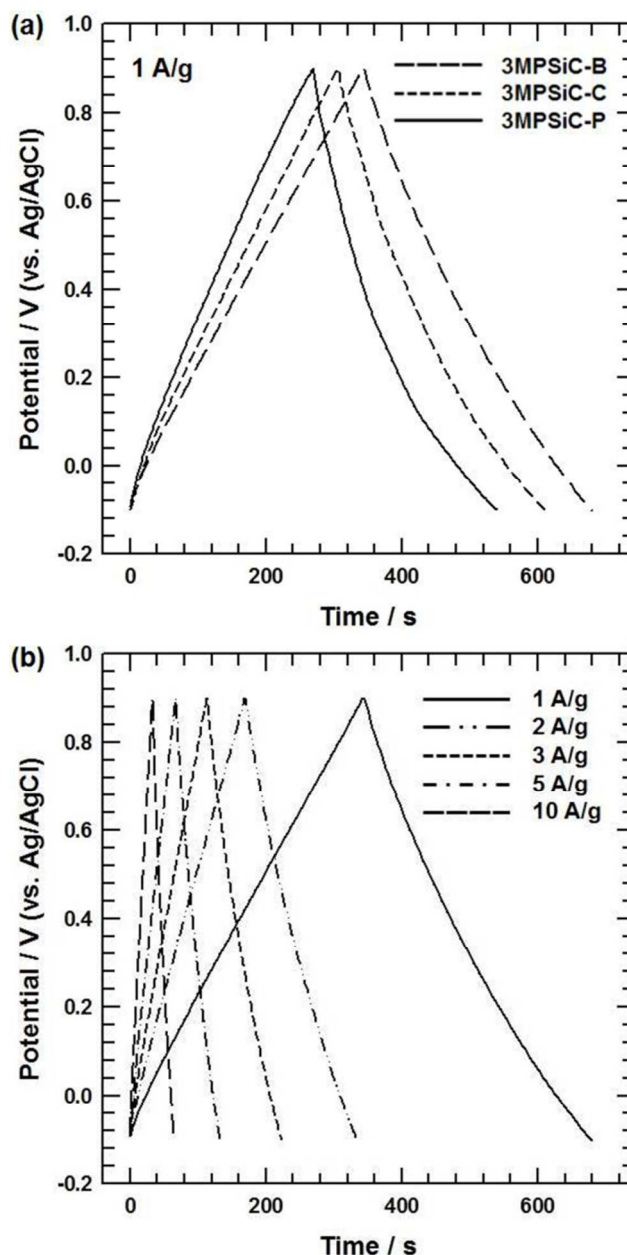
Figure 6. (a) Galvanostatic charge/discharge curves for 3MPSiC-C, 3MPSiC-B and 3MPSiC-P electrodes at a current density of 1 A g^{-1}. (b) Galvanostatic charge/discharge curves of 3MPSiC-B electrode at different current densities.

3MPSiC-B electrode, relative to the 3MPSiC-C and 3MPSiC-P electrodes, implying that the specific capacitance is highest for the

3MPSiC-B electrode, which is consistent with the results of the CV analysis. The rapid charge-discharge properties were evaluated by detailed analysis of the 3MPSiC-B electrode. Figure 6(b) shows the galvanostatic charge/discharge curves of the 3MPSiC-B electrode at different current densities. All of the curves are highly linear and symmetric with increasing current density, indicating that the 3MPSiC-B electrode has excellent electrochemical reversibility and charge-discharge properties.[49] Generally, a sudden potential drop at the very beginning of the constant current discharge is observed for EDLCs, and this drop has been designated as the IR drop. This potential drop has been attributed to the resistance of the electrolytes and the inner resistance of electrolyte ion migration in porous electrode materials. The latter usually constitutes a greater contribution to the overall IR drop.[50] The IR drop is similar for all curves and is not pronounced even at 10 A g^{-1}, indicating little overall resistance and excellent capacitive properties of the 3MPSiC-B electrode due to the interconnected micro-, meso-, and macroporous structure.
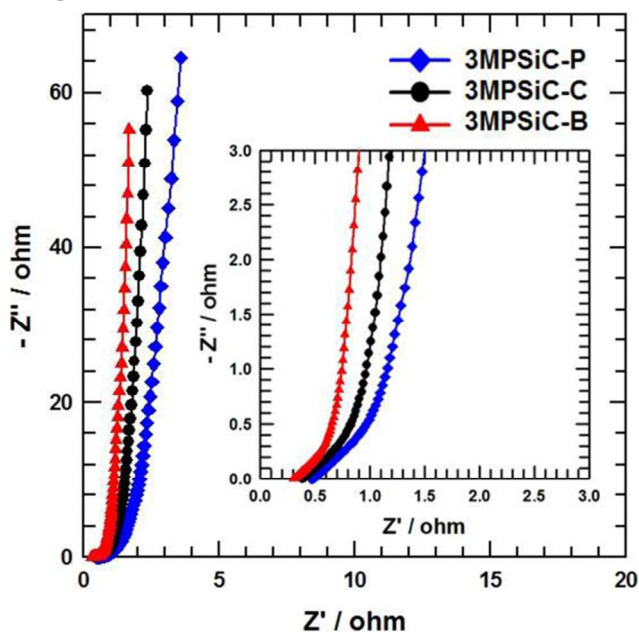
Figure 7. Nyquist plots for 3MPSiC-C, 3MPSiC-B and 3MPSiC-P electrodes. Inset magnifies the data in the high-frequency range.

EIS measurements were performed for the 3MPSiC-C, 3MPSiC-B, and 3MPSiC-P electrodes, as shown in Figure 7. The EIS data was analyzed using Nyquist plots. Nyquist plots show the frequency response of the 3MPSiC electrode/electrolyte system and are a plot of the imaginary component (Z") of the impedance against the real component (Z'). The Nyquist plots consist of three parts: (i) the intersection of the curve at the X-axis represents the internal or equivalent series resistance (ESR); (ii) a straight line with a slope of 45° in the low-frequency range, which corresponds to the semi-infinite Warburg impedance resulting from the frequency dependence of ion diffusion/transport in the electrolyte; (iii) a vertical line at very low frequencies, caused by the accumulation of ions at the bottom of the pores of the electrode. The nearly vertical line indicates good capacitive behavior without diffusion limitations.[51,52] All of the 3MPSiC electrodes show the low value of

the intercept of the real axis with negligible charge transfer resistance in high-frequency range due to the excellent electrical conductivity which can greatly decrease the internal resistance of an electrode by the construction of a conductive network. In comparing the 3MPSiC-C, 3MPSiC-B and 3MPSiC-P electrodes, the major difference is observed in the Warburg and vertical line region in the low-frequency range. Among these three 3MPSiC electrodes, the 3MPSiC-B electrode shows the shortest Warburg region and the largest slope of vertical curve with respect to the Z' axis in the Nyquist plot. This result can be attributed to the ideal mesopore size of 3MPSiC-B electrode, which can enable the fast ion diffusion in the electrolyte and ion adsorption onto the electrode surface and reduce the resistant pathways for ion diffusion in the pores.
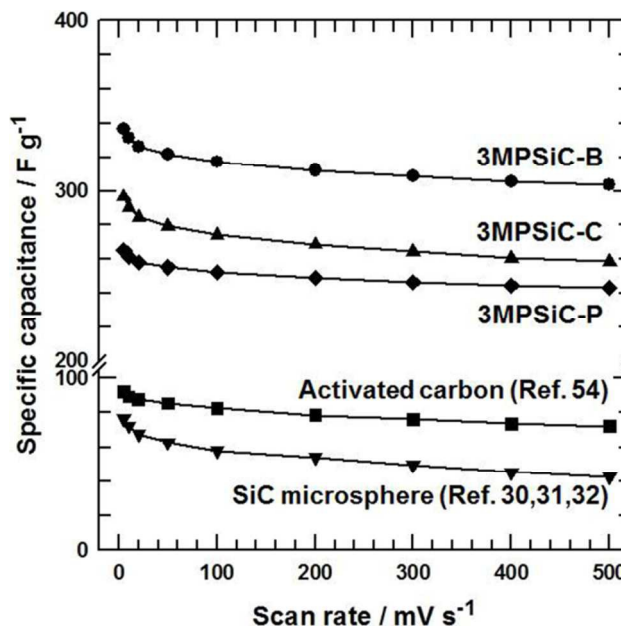
Figure 8. Specific capacitances for 3MPSiC-C, 3MPSiC-B and 3MPSiC-P electrodes at different scan rates, the data used for comparison were calculated from the capacitance data given in the corresponding references.

The specific capacitances (C_s) are calculated from the CV curves using the following equation:[53]

$$C_s = \frac{1}{v(V_c - V_a)} \int_a^c I(V)dV \qquad (1)$$

where C_s is the specific capacitance (F g^{-1}), v is the potential scan rate (mV s^{-1}), $V_c - V_a$ represents the sweep potential range (V), and $I(V)$ denotes the response current density (A g^{-1}). Figure 8 shows the specific capacitance of the 3MPSiC-C, 3MPSiC-B, and 3MPSiC-P electrodes as a function of the scan rate. The capacitive performances of silicon carbide microsphere which is non-porous structure and activated carbons that mainly comprise micropores were compared with that of the 3MPSiC electrodes to investigate the effect of the pore structure.[30-32,54] The calculated C_s values of the 3MPSiC-C, 3MPSiC-B, and 3MPSiC-P electrodes at a scan rate of 5 mV s^{-1} are 296.7, 336.5, and 265.2 F g^{-1}, respectively. Moreover, the C_s values for all of the electrodes decreased steadily with increasing scan rate owing to the reduced access of ions to the active

surface. However, the capacitance retention in response to the scan rate increase from 5 to 500 mV s^{-1} of the 3MPSiC-B electrode (90.3 %) is lower than that of the 3MPSiC-P (91.8 %) electrode, which can be attributed to the smaller mesopore size of the former. The bigger pore size is beneficial for fast ion transport through the porous network, especially when a large loading current density is employed.[36] Importantly, the C_s values for all 3MPSiC electrodes were significantly higher than that of the silicon carbide microsphere and activated carbon electrodes over the entire range of scan rate due to the synergistic effect that concomitantly strengthened the electric double-layer properties derived from the micropores, reduced the resistant pathways for ion diffusion in the pores caused by the mesopores, and greatly diminished the ion-wall collision phenomenon as well as the formation of ion buffering reservoirs due to macropores. Moreover, in these ternary porous systems, the macropores can play an important role for the electrolyte ion transportation. Generally, ion transport involves two main interaction pairs: ion-ion and ion-wall. The former is determined by the electrolyte concentration and is pore diameter independent; the latter depends on the ratio of the pore diameter to the ion diameter. According to previous reports, when the ratio of the pore diameter to the ion diameter is greater than 20, the collision probability in ion-wall interactions is close to zero because the nanopores are large enough (larger than 10 nm) to avoid collisions between ion and wall. Thus, considering the large size of the macropores in the 3MPSiC samples, ion-wall collisions may be greatly diminished in this system and the electrolyte ions assume bulk-phase behavior in these pores, resulting in rapid transport behavior.[33,55,56] Therefore, based on these encouraging results, the micro-, meso- and macroporous SiC can be a promising new EDLC material for supercapacitors, and opens up new possibilities for the fabrication of other porous inorganic materials for energy storage devices.

4. Conclusion

In summary, hierarchical micro-, meso-, and macroporous silicon carbide (3MPSiC) spheres were synthesized via a template method followed by carbonization via an aerosol spray drying method. The 3MPSiC electrode prepared by using Brij56 as a structure directing agent for the mesopore template and PSL spheres as the macropore template exhibited the highest charge storage capacity with a specific capacitance of 336.5 F g^{-1} at a scan rate of 5 mV s^{-1} with a rate performance of 90.3 % from 5 to 500 mV s^{-1} in 1 M Na$_2$SO$_4$ aqueous electrolyte. This outstanding electrochemical performance can be attributed to the synergistic effect of the ternary-pore system, in which macropores form a bulk buffering reservoir for electrolytes, mesopores provide a large accessible surface area for ion transport/charge storage, and micropores continuously increase the charge accommodation.

Acknowledgements

Notes and references

School of Chemical Engineering & Materials Science, Chung-Ang University, 84 Heukseok-Ro, Dongjak-gu, Seoul 156-756, Korea.
E-mail : jooheonkim@cau.ac.kr
Phone : +82-2-820-5763, Fax : +82-2-824-3495

1. A.L. Mohana, R.F. Estaline, A. Imran and J.S. Ramaprabhu, *Nanoscale Res. Lett.*, 2008, **3**, 145-151.
2. A.C.-G. Karina, L.-C. Monica, C.-P. Nieves and G.-R. Pedro, *Adv. Funct. Mater.*, 2005, **15**, 1125-1133.
3. V. Subramanian, H. Zhu, R. Vajtai, P.M. Ajayan and B. Wei, *J. Phys. Chem. B.*, 2005, **109**, 20207-20214.
4. R. Kotz and M. Carlen, *Electrochim. Acta*, 2000, **45**, 2483-2498.
5. Z. Chen, Y. Qin, D. Weng, Q. Xiao, Y. Peng, X. Wang, H. Li, F. Wei and Y. Lu, *Adv. Funct. Mater.*, 2009, **19**, 3420-3426.
6. J. Chow, R.J. Kopp and P.R. Portney, *Science*, 2003, **302**, 1528-1531.
7. Z. Wen, X. Wang, S. Mao, Z. Bo, H. Kim, S. Cui, G. Lu, X. Feng and J. Chen, *Adv. Mater.*, 2012, **24**, 5610-5616.
8. S. Bose, T. Kuila, A.K. Mishra, R. Rajasekar, N.H. Kim and J.H. Lee, *J. Mater. Chem.*, 2012, **22**, 767-784.
9. H. Jiang, J. Ma and C.Z. Li, *Adv. Mater.*, 2012, **24**, 4197-4202.
10. M. Armand, F. Endres, D. R. MacFarlane, H. Ohno and B. Scrosati, *Nat. Mater.* 2009, **8**, 621–629.
11. T. Kim, G. Jung, S. Yoo, K.S. Suh and R.S. Ruoff, *ACS Nano*, 2013, **7**, 6899-6905.
12. J. Chmiola, G. Yushin, Y. Gogotsi, C. Portet, P. Simon and P. L. Taberna, *Science*, 2006, **313**, 1760–1763.
13. C. Portet, M. A. Lillo-Rodenas, A. Linares-Solano and Y. Gogotsi, *Phys. Chem. Chem. Phys.* 2009, **11**, 4943–4945.
14. R. Dash, J. Chmiola, G. Yushin, Y. Gogotsi, G. Laudisio, J. Singer, J. Fischer and S. Kucheyev, *Carbon*, 2006, **44**, 2489–2497.
15. W. Xing, S. Z. Qiao, R. G. Ding, F. Li, G. Q. Lu, Z. F. Yan and H. M. Cheng, *Carbon*, 2006, **44**, 216–224.
16. K. Jurewicz, C. Vix-Guterl, E. Frackowiak, S. Saadallah, A. Reda, J. Parmentier, J. Patarin and F. Beguin, *J. Phys. Chem. Solids*. 2004, **65**, 287–293.
17. R. W. Pekala, J. C. Farmer, C. T. Alviso, T. D. Tran, S. T. Mayer, J. M. Miller and B. Dunn, *J. Non-Cryst. Solids* 1998, **225**, 74–80.
18. L.L. Zhang, R. Zhou and X.S. Zhao, *J. Mater. Chem.*, 2010, **20**, 5983-5992.
19. X.C. Dong, H. Xu, X.W. Wang, Y.X. Huang, M.B.C. Park, H. Zhang, L.H. Wang, W. Huang and P. Chen, *ACS Nano*, 2012, **6**, 3206-3213.
20. S. Chen, J. Zhu and X. Wang, *J. Phys. Chem. C.*, 2010, **114**, 11829-11834.
21. X. Xia, Q. Hao, W. Lei, W. Wang, D. Sun and X. Wang, *J. Mater. Chem.*, 2012, **22**, 16844-16850.
22. C. Xiang, M. Li, M. Zhi, A. Manivannan and N. Wu, *J. Power Sources*, 2013, **226**, 65-70.
23. B. Zhao, P. Liu, Y. Jiang, D. Pan, H. Tao, J. Song, T. Fang and W. Xu, *J. Power Sources*, 2012, **108**, 423-427

24. J.W. Choi, J. McDonough, S. Jeong, J.S. Yoo, C.K. Chan and Y. Cui, *Nano Lett.*, 2010, **10**, 1409-1413.

25. J.P. Alper, M. Vincent, C. Carraro and R. Maboudian, *Appl. Phys. Lett.*, 2012, **100**, 163901-163904.

26. J.P. Alper, M.S. Kim, M. Vincent, B. Hsia, V. Radmilovic, C. Carraro and R. Maboudian, *J. Power Sources*, 2013, **230**, 298-302.

27. X. Lu, G. Wang, T. Zhai, M. Yu, S. Xie, Y. Ling, C. Liang, Y. Tong and Y. Li, *Nano Lett.*, 2012, **12**, 5376-5381.

28. X. Lu, G. Wang, T. Zhai, M. Yu, J. Gan, Y. Tong and Y. Li, *Nano Lett.*, 2012, **12**, 1690-1696.

29. H. Zhang, T. Zhai, M. Yu, S. Xie, C. Liang, W. Zhao, S.C.I. Wang, Z. Zhang and X. Lu, *J. Mater. Chem. C*, 2013, **1**, 225-229.

30. M. J. Kim, Y. J. Yoo, and J. H. Kim, *J. Power Sources*, 2014, **265**, 214-222.

31. M. J. Kim and J. H. Kim, *Phys. Chem. Chem. Phys.* 2014, **16**, 11323–11336.

32. M. J. Kim and J. H. Kim, *ACS Appl. Mater. Interfaces*, 2014, **6**, 9036−9045.

33. F. Xu, R. Cai, Q. Zeng, C. Zou, D. Wu, F. Li, X. Lu, Y. Liang and R. Fu, *J. Mater. Chem.*, 2011, **21**, 1970-1976.

34. Z.S. Wu, Y. Sun, Y.Z. Tan, S. Yang, X. Feng and K. Mullen, *J. Am. Chem. Soc.* 2012, **134**, 19532−19535.

35. D.W. Wang, F. Li, M. Liu, G.Q. Lu and H.M. Cheng, *Angew. Chem. Int. Ed.* 2008, **47**, 373–376.

36. W. Xiong, M. Liu, L. Gan, Y. Lv, Z. Xu, Z. Hao and L. Chen, *Colloids and Surfaces A: Physicochem. Eng. Aspects*, 2012, **411**, 34–39.

37. Z.Y. Yuan and B.L. Su, *J. Mater. Chem.*, 2006, **11**, 663-677.

38. Y. Lu, H. Fan, A. Stump, T.L. Ward, T. Rieker and C.J. Brinker, *Nature*, 1999, **398**, 223-226.

39. N.M. Vinothan, I. Arnout, D.T. James and J.P. David, *Adv. Mater.*, 2001, **13**, 447-450.

40. Y. Yang, G. Meng, X. Liu, L. Zhang, Z. Hu, C. He and Y. Hu, *J. Phys. Chem. C.*, 2008, **112**, 20126-20130.

41. Y. Zhang, E.W. Shi, Z.Z. Chen, X.B. Li and B. Xiao, *J.Mater.Chem.*, 2006, **16**, 4141-4145.

42. Z. Liu, L. Ci, N.Y. Jin-Phillipp and M. Ruhle, *J. Phys. Chem. C.*, 2007, **111**, 12517-12521.

43. J.B. Casady and R.W. Johnson, *Solid-State Electron.*, 1996, **39**, 1409-1422.

44. K. Shimoda, J.S. Park, T. Hinoki and A. Kohyama, *Appl. Surf. Sci.* 2007, **253**, 9450-9456.

45. R. Liu, B. Liu, K. Zhang, M. Liu, Y. Shao and C. Tang, *J. Nucl. Mater.* 2014, **453**, 107-114.

46. M. J. Kim, Y. S. Hwang and J. H. Kim, *J. Power Sources*, 2013, **239**, 225-233.

47. W. Qian, F. Sun, Y. Xu, L. Qiu, C. Liu, S. Wang and F. Yan, *Energy Environ. Sci.* 2014, **7**, 379-386.

48. M. J. Kim, Y. S. Hwang and J. H. Kim, *Phys. Chem. Chem. Phys.* 2014, **16**, 351–361.

49. L. Z. Fan, Y. S. Hu, J. Maier, P. Adelhelm, B. Smarsly and M. Antonietti, *Adv. Funct. Mater.*, 2007, **17**, 3083–3087.

50. C.T. Hsieh and H. Teng, *Carbon*, 2002, **40**, 667-674.

51. M.D. Stoller, S.J. Park, Y. Zhu, J.H. An, and R.S. Ruoff, *Nano Lett.*, 2008, **8**, 3498-3502.

52. L. Lai, H. Yang, L. Wang, B.K. Teh, J. Zhong, H. Chou, L. Chen, W. Chen, Z. Shen, R.S. Ruoff and J. Lin, *ACS Nano*, 2012, **6**, 5941-5951.

53. X. Xie and L. Gao, *Carbon*, 2007, **45**, 2365-2373.

54. M. J. Kim, Y. S. Hwang, and J. H. Kim, *Electrochim. Acta*, 2013, **113**, 322-331.

55. H. J. Liu, W. J. Cui, L. H. Jin, C. X. Wang and Y. Y. Xia, *J. Mater. Chem.*, 2009, **19**, 3661–3667.

56. D. W. Wang, F. Li, M. Liu, G. Q. Lu and H. M. Cheng, *J. Phys. Chem. C*, 2008, **112**, 9950–9955.